RESEARCH ARTICLE | DECEMBER 05 2025

Experimental and simulation study on high-power laser irradiation of 3D-printed microstructures

M. Cipriani ; F. Consoli ; M. Scisció ; A. Solovjovas ; I. A. Petsi; M. Malinauskas ; P. Andreoli; G. Cristofari ; E. Di Ferdinando; G. Di Giorgio

Matter Radiat. Extremes 11, 027401 (2026)
https://doi.org/10.1063/5.0283201

Matter and Radiation at Extremes

RESEARCH ARTICLE

pubs.aip.org/aip/mre

Experimental and simulation study on high-power laser irradiation of 3D-printed microstructures

Cite as: Matter Radiat. Extremes 11, 027401 (2026); doi: 10.1063/5.0283201
Submitted: 30 May 2025 • Accepted: 10 November 2025 •
Published Online: 5 December 2025

M. Cipriani,[1,a] F. Consoli,[1] M. Scisció,[1] A. Solovjovas,[2] I. A. Petsi,[2] M. Malinauskas,[2] P. Andreoli,[1] G. Cristofari,[1] E. Di Ferdinando,[1] and G. Di Giorgio[1]

AFFILIATIONS

[1] ENEA, Nuclear Department, Centro Ricerche Frascati, Frascati, Italy
[2] Laser Nanophotonics Group, Laser Research Center, Physics Faculty, Vilnius University, Vilnius, Lithuania

[a] **Author to whom correspondence should be addressed:** mattia.cipriani@enea.it

ABSTRACT

Inertial confinement fusion (ICF) requires a constant search for the most effective materials to improve the efficiency of compression of the capsule and of laser-to-target energy transfer. Foams could provide a solution, but they require further experimental and theoretical investigation. The new 3D-printing technologies, such as two-photon polymerization, are opening a new era in the production of foams, allowing fine control of material morphology. Very few detailed studies of the interaction of foams with high-power lasers in regimes relevant for ICF have been described in the literature to date, and more investigation is needed. In this work, we present the results of an experimental campaign performed at the ABC laser facility at ENEA Centro Ricerche Frascati in which 3D-printed microstructured materials were irradiated at high power. 3D simulations of the laser–target interaction performed with the FLASH code reveal that the laser is scattered by plasma density gradients and channeled into the structure when the center of the focal spot is on the through hole. The time required for the laser to completely ablate the structure given by the simulations is in good agreement with the experimental measurement. Measurements of the reflected and transmitted laser light indicate that scattering occurred during the irradiation, in accordance with the simulations. Two-plasmon decay has also been found to be active during irradiation.

I. INTRODUCTION

The peculiar way in which high-power lasers interact with microstructured materials, or foams, and the evolution of the plasma generated by the laser action have proved to be useful for various applications. Foams have been used as efficient sources of X rays,[1] for the study of shock waves[2] and equations of state (EoS),[3] for efficient particle acceleration and neutron and betatron generation with short laser pulses.[4] In particular, foams find many applications in inertial confinement fusion (ICF), because of their ability to enhance laser absorption,[5] smooth laser inhomogeneities in the transverse energy profile,[6] and enhance the ablation loading on a substrate.[7] Recently, low-density foams have been found to reduce stimulated Brillouin scattering (SBS) instability, which has been linked to an increased ratio between ion and electron temperatures.[8,9] Their use inside hohlraums has been suggested to prevent wall expansion[10,11] and to function as support materials for liquid nuclear fuel, as "wetted foams".[12,13] Recent advances in manufacturing, simulation, and diagnostics are opening the way to a deeper and more fundamental investigation of the characteristics of the plasma generated by the action of high-power lasers.

Until a few years ago, foams of light elements were manufactured through chemical processes, creating a gel, and then removing the solvent from it (see, e.g., Ref. 14 for a review). We refer to the foams produced in this way as *chemical* foams. These foams are convenient because of their low price per sample and because they can be realized in a large number in a short time. On the other hand, their structural parameters, such as pore size, solid part thickness, and average density, can be precisely controlled only within some ranges of values, and they may vary from sample to sample because of the intrinsic stochasticity of the production process. Moreover, the manipulation of these materials during manufacturing and in

experiments often poses serious difficulties, owing to the softness and fragility of the structure, especially at densities lower than 10 mg/cm^3. Now, however, Laser Direct Writing (LDW) Multi-Photon 3D lithography (MP3DL) based on two-photon polymerization (see, e.g., Refs. 15 and 16 for an extensive review and tutorials) allows the production of innovative foam samples with a predictable and reproducible structure, useful for laser–matter experiments.[17,18] The technique is particularly attractive for rapid prototyping of high-resolution complex architectures for experimental research requiring advanced material engineering.[19] Furthermore, recent developments toward increasing throughput up to 10^7 voxels/s have given results that are very promising for scaling up the production rate to a level suitable for mass-customized manufacturing.[20] In particular, LDW allows precise design of sample morphology, which can in principle be engineered for any experimental need, improving not only its performances but also the diagnostics of the laser-produced plasma. Producing a rather limited amount of high-quality samples, however, still requires several hours, which is reflected in a high price per sample. This technology has been available for a few years, and it has scope for new developments that could enable the manufacture of foams with the parameters required for the applications listed above. For smoothing laser energy deposition or enhancing particle acceleration, foam densities should be of the order of 10 mg/cm^3 or lower, with pore sizes below 1 μm.[4,6] In this parameter range, the thickness of the solid parts is constrained to be of the order of tens of nanometers. However, at present, the lowest achievable thickness of 3D printed filaments is of the order of 100 nm, but in general is at most about 500 nm to ensure stability of the sample. With this constraint, the lower bound on the average energy density obtainable with 3D printing is about 10 mg/cm^3,[17] but with a separation of the order of 10 μm. On the other hand, making foams with larger densities above 50 mg/cm^3, with pore sizes of the order of a few micrometers, is less demanding. For this range of parameters, different foam morphologies can be explored, such as body-centered, octet truss, or Voronoi lattice,[13,17,18] which could lead to smoother shock fronts and higher-performance implosions in the future. Such high densities, of the order of hundreds of milligrams per cubic centimeter, are required, for example, for studying hydrodynamic surrogates of wetted foams[13,21] or for laboratory astrophysics experiments.[22]

The simulation of the interaction of a high-power laser beam with such materials is a challenging task, owing to the different scales of the foam morphology. As mentioned above, for chemical foams, the filament thickness ranges from tens to hundreds of nanometers, while the pore size goes from a few to tens of micrometers. The stochasticity of the structure adds even more difficulties to the modeling. To computationally resolve this problem, several subgrid models have been implemented in radiation-hydrodynamics codes.[23–26] The advantage of using these models is that their implementation in the codes does not appreciably change the computational performance of the original code. On the other hand, the models necessarily approximate the physics involved in the plasma evolution and can lack accuracy. Simulations exploiting a more fundamental description of the laser–matter interaction would be preferable. Recent technological advances in target manufacturing, simulation codes, and computational hardware allow this approach to be adopted. On the one hand, printed foams can have regular structures that can in principle be replicated in numerical codes with a one-to-one correspondence, which is not feasible for the nonregular structures of chemical foams. On the other hand, the development of parallel radiation-hydrodynamics codes and advances in high-performance computing (HPC) infrastructures has enabled a growth in computational power, allowing more demanding simulations to be run in a reduced time.[27]

In this work, we present the results of an experimental campaign performed at the ABC laser facility at the ENEA Research Center at Frascati for high-power irradiation of additively manufactured materials. Our work represents an addition to the few previous numerical and experimental efforts[13,18,28,29] devoted to the study of the behavior of printed foams under irradiation by high-power laser pulses. We used tailored microstructured samples with a log-pile structure obtained through LDW with the SZ2080 hybrid pre-polymer, supported by a holder 3D-printed with UV stereolithography, specifically designed to allow optimal access to the diagnostics fielded in the experiments. All structural parameters, apart from the thickness, were the same across the whole set of samples, to ensure the highest possible shot-to-shot reproducibility. We irradiated these samples at intensities from 10^{14} to about 10^{15} W/cm^2, to investigate the behavior of the laser-generated plasma, focusing in particular on the speed at which the material was eroded by the laser action, the ablation of the solid parts, and the absorption efficiency. Such intensities are of interest for ICF research, being of the same order of magnitude as those used in direct drive experiments.[30–32] The laser wavelength was the fundamental Nd:glass harmonic at 1054 nm, which was chosen to maximize the laser energy on the target and thus to reach the highest possible intensities. This allowed us to increase the ablation pressure in the plasma and to enhance the effects of laser–plasma instabilities (LPIs), by lowering the excitation thresholds. We performed 3D radiation-hydrodynamics simulations with the FLASH code, in which the target microstructure was directly reproduced, exploiting the parallelization capabilities of the code on the HPC cluster ENEA-CRESCO6.[33] The thickness of the filaments and their separation in the targets used in the experiment were chosen to lower the computational cost for 3D simulations, having a coarse structure, and to ease sample production. This lengthened the time required to fill the gaps between the filaments, thus enhancing the effects of some physical processes that would otherwise be less evident, such as the laser scattering in the sample due to refraction in the plasma generated from heating of the filaments. The log-pile morphology was selected to reduce the complexity of material fabrication, in favor of the quality of the final result. Future foams for fusion targets would need to have more random morphologies, to reduce the appearance of asymmetries during compression, particularly when the foam constitutes the whole capsule, as in Ref. 13. However, the irradiation of regular structures in planar geometry is relevant for understanding the fundamental physical processes involved, while keeping the manufacturing complexity low and allowing a direct representation of the sample in hydrocodes, as is done in this work.

II. TARGETS

The samples used in the experiments were composed of two parts, printed with different techniques, as shown in Fig. 1. The holders were produced using a table-top 3D UV printer and Asiga Plasgray photo-resin to support the log-piles during manufacture,

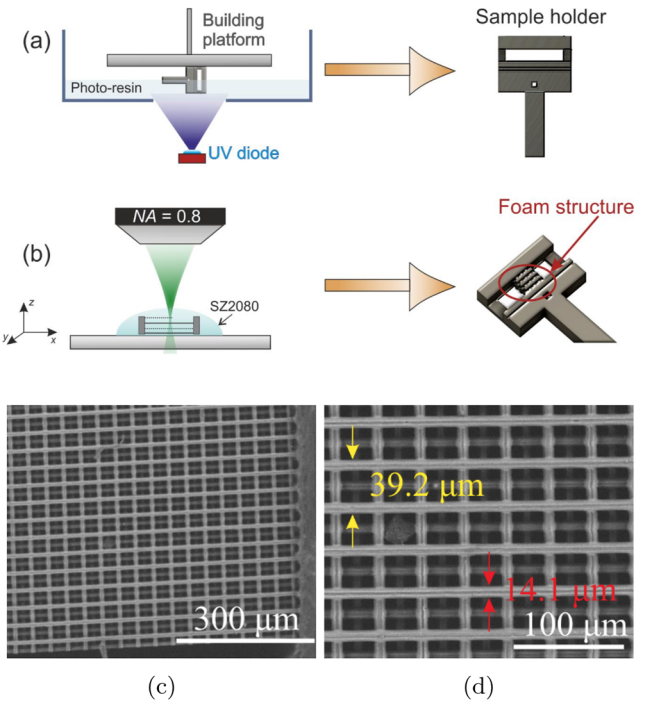

FIG. 1. Illustrations of techniques for production of (a) target holders and (b) microstructures. Scanning electron microscopy images of the samples used in the experiments with (c) 250× and (d) 600× (d) magnifications. In (d), the filament separation is indicated in yellow and the filament thickness in red.

avoiding deformations of the structures, and for handling in the experimental chamber during irradiation. The shape of the holder was designed to allow optimal access to the diagnostics used in the experiment, described in Sec. III. The microstructures were fabricated with a LDW MPL3DL printer directly into the holders, using SZ2080 hybrid pre-polymer. This pre-polymer contains Si and Zr, with chemical formula $C_4H_{12}SiZrO_2$. We estimated that in the final structure, the percentage by mass of Si atoms was about 15%, while that of Zr atoms was about 24%. The separation between the filaments was 39.2 μm, and the filament thickness was 14.1 μm over the whole structure, with an average density of 348 mg/cm^3. As noted in Sec. I, this density is in the range of the hundreds of mg/cm^3 required for using foams as hydrodynamic surrogates of wetted foams, as in Ref. 21. To increase the cross-section of interaction with the main laser beam under irradiation, we printed the layers in the log-pile with a shift of one-half of the period of the structure in both directions. Each sample had a square transverse shape with sides of 500 μm and a variable thickness ranging from about 100 to 400 μm. Additional details of the fabrication process can be found in Appendix A.

III. EXPERIMENT

The results discussed in this work are from a recent experimental campaign carried out at the ABC laser facility at the ENEA Centro Ricerche Frascati. ABC is a Nd:glass laser capable of delivering two counter-propagating beams with a wavelength of 1054 nm and a maximum energy of 100 J each. For this experiment, we used a single-beam configuration in a planar irradiation geometry. The temporal shape of the pulse was a $\sin^2 t$ with a full duration of 5 ns, 3 ns full width at half maximum, and a total energy of about 40 J. The pulse energy was maintained as constant as possible among the different shots, in order to assess the repeatability of the experimental results. The beam was focused on the target at normal incidence using an $f/1$ lens. Two focal spot diameters were used, namely, 50 and 100 μm, resulting in lower and maximum intensities of $I_{lower} = 1.3 \times 10^{14}$ W/cm^2 and $I_{max} = 7 \times 10^{14}$ W/cm^2, respectively. The laser energy in the spot had a Gaussian distribution.

A sketch of the experimental setup is shown in Fig. 2. The laser temporal profile was monitored for each shot by a calibrated photodiode (photodiode L). The laser light reflected by and transmitted through the target was collected by the two focusing lenses A and B with the following method. The main beam light was linearly polarized, passed through a polarizer with the same orientation, and entered the interaction chamber through a $\lambda/4$ plate, which changed the polarization from linear to circular. The light reflected by the target and intercepting the focusing lens exited the chamber, passing through the same $\lambda/4$ plate, and its circular polarization was turned into linear again, but in an orthogonal direction with respect to the incoming laser light, thus being rejected by the polarizer and collected by the photodiode R. On the other hand of the chamber, a mirror version of this setup was in place, and photodiode T then collected the laser light transmitted through the target. A green probe beam with a wavelength of 527 nm and a time duration of 500 ps was generated by picking a small portion of the main beam light along the amplification path and frequency-doubling it, so that it was absolutely synchronized with the main beam. The probe beam was delayed with respect to the main beam by 12 ns. A Hamamatsu C5680 visible streak camera observed the target from the side, to record the self-emitted light from the plasma generated at the front and at the back of the target. Each pixel of the CCD camera of the readout system covered a range in time of about 18 ps and a range in space of about 1.4 μm. The error in the post-processing of

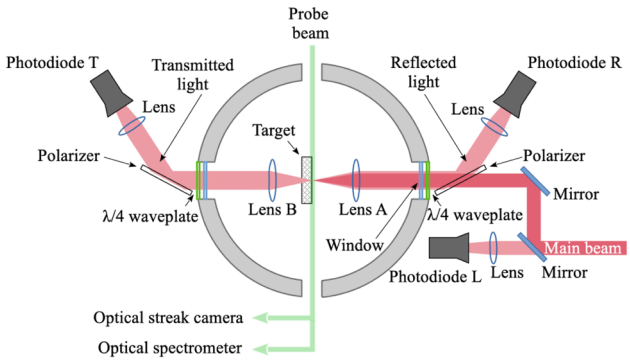

FIG. 2. Experimental setup. The pulse temporal profile was monitored by the fast photodiode L, collecting a leak from a mirror on the laser optical path. The laser light reflected and transmitted by the target was collected by the focusing lenses and detected by the two fast photodiodes R and L. A visible streak camera imaged the light self-emitted by the plasma at 90° from the laser propagation direction. At the same position, a visible spectrometer was used to spectrally resolve the plasma self-emission.

the images was larger, as discussed later in Sec. IV C. The streak slit was 40 μm wide on the final streaked image. The probe beam reached the slit of the streak camera, thus acting as a time fiducial on the streaked image. A Ocean Optics HR4000 spectrometer collected the self-emitted light from the plasma in the visible range in a time-integrated manner.

IV. SIMULATION RESULTS

Before discussing the experimental outcomes, we present the results of the numerical simulations, which clarify the hydrodynamic behavior of the material under irradiation, in particular regarding the degree of homogenization of the plasma. As we will see in Sec. IV C, owing to the large thickness of the filaments, the plasma does not reach the homogenization. Therefore, we cannot speak about a shock wave being generated in the material, and we will refer to the propagation of the front of the region where the microstructure has been ablated as an *erosion* wave.

A. Simulation parameters

To simulate the behavior of the material under irradiation, we used the FLASH code.[34,35] FLASH is an open-source modular multiphysics code in which the plasma fluid equations are solved with finite-volume methods on an Eulerian grid. The code has adaptive mesh refinement (AMR) capabilities, implicit solvers for diffusion, laser ray-tracing, radiation diffusion, and multimaterial support with tabulated equations of state (EoS) and opacities. All the simulations were run on the ENEA CRESCO high-performance computing infrastructure.[33] The large filament thickness and interfilament spacing allowed us to directly reproduce the sample structure in the code as the initial condition and complete the simulation in a reasonable time, thereby avoiding approximations or specific modeling for describing the plasma evolution. The mesh was chosen as static rectangular with a cell size of about 1 μm in each spatial direction. Such a resolution allowed us to properly resolve the shock dynamics inside the filaments. To assess the stability of the simulations in terms of the mesh resolution, we ran two test cases in the 100C configuration (see Sec. IV B), one with 2 μm and one with 0.5 μm resolution. Although the plasma density profile was not exactly the same, owing to the lower or higher detail resolved by the code with the coarser or finer mesh, the difference in the speed at which the material was eroded by the laser action, which was our main experimental observable, was very small among those cases. To keep the computational cost as low as possible, without sacrificing accuracy, we used 1 μm resolution for all the other simulations reported in this work. We discuss this issue in more detail in Appendix B 1. We did not exploit the AMR capabilities of the FLASH code, since the refinement process for such a large number of cells would have impacted performance. In fact, with the very inhomogeneous plasma rapidly filling almost the whole domain from the very beginning of the simulation, the most refined mesh would have been required everywhere, thus not improving performance compared with a static mesh. The 3D ray tracing available in the FLASH code allowed us to reproduce the angular incidence of the ABC laser beam on the sample and its scattering on the filaments due to refraction by the plasma at the beginning of the interaction, before the closure of the empty spaces due to the plasma fill. To properly model the laser absorption and diffusion into the structures, we set the number of rays to 10^4 in the ray tracing package. We tested the reliability of this choice by running a simulation in case 100C (see Sec. IV B) with four times more rays, i.e., twice as many rays per dimension in the 2D plane of the focal spot. The plasma quantity profiles for this latter case were almost indistinguishable from the former, indicating that 10^4 rays were enough to resolve the laser propagation. We describe this in detail in Appendix B 2. The EoS used for modeling the material under study was 7592 from the SESAME database.[36] This EoS has been tested in experiments involving trimethylolpropane triacrylate (TMPTA) foam in Ref. 21, and good agreement with these experiments was found. Since no specific EoS for SZ2080 is available, we assume that this EoS is able to capture the overall features of the behavior of the material under compression in our problem. For comparison, we ran all the simulations with the EoS for polystyrene obtained by the IONMIX code.[37] The simulations gave similar results with both EoS, even though some differences can be identified, as we will discuss below. The density of the filaments was set to be 1.2 g/cm^3, in accordance with the density of the printed material. As discussed in Sec. II, the printed structures contained Si and Zr and the role played by radiation should in principle be accounted for in the simulations. The mass percentages of Zr and Si in the SZ2080 pre-polymer are 48% and 15%, respectively. However, as indicated in Sec. II, the estimated percentages are 24% and 15%, respectively. Therefore, we can assume the final chemical formula of the material to be $C_8H_{24}Si_2ZrO_4$. We used this formula to obtain the opacities from the TOPS website.[38] Since Zr is not available in the TOPS database, we replaced it with Zn, being the element with the highest Z number available. We chose the temperature range 0.001–10 keV, with 33 values, and the density range 0.001–10.0 g/cm^3 with 20 values, with six radiation groups. Owing to the high computational cost of including radiation transport, we compared a simulation with radiation transport with another without it in case 100C (see Sec. IV B), to assess the extent to which this played a role in the plasma evolution in our specific experimental situation. The inclusion of radiation showed a pre-heating of the structure ahead of the erosion wave front, causing some degree of pre-expansion of the filaments. The value of the temperature in the ablated region in the case without radiation looked more uniform, while in the case with radiation included, the hotter part of the plasma was confined to the focusing cone of the laser, where the energy losses were compensated by laser energy deposition. However, the difference between the two cases in the speed of the erosion wave, which was our main experimental observable, as discussed in Sec. V, was limited to about 2.3%. We found this discrepancy small enough to run all the simulations in this work without radiation, reducing the computation times by a factor of about three.

B. Laser pointing and laser scattering

The initial setup of the simulation is shown in Fig. 3. We used the two focal spot diameters mentioned in Sec. III, namely, 50 and 100 μm. The 50 μm diameter was of the same order as the separation between the filaments in each single layer, while the 100 μm diameter could completely cover a square of four elementary cells. For each focal spot size, we can identify two limiting cases in terms of the position of the center of the spot, as depicted in Fig. 4. Since we used an $f/1$ lens in the experiments, distinguishing between these two cases has an important relevance, as we will see shortly. We will henceforth refer to each of these cases with the following labels: 100C,

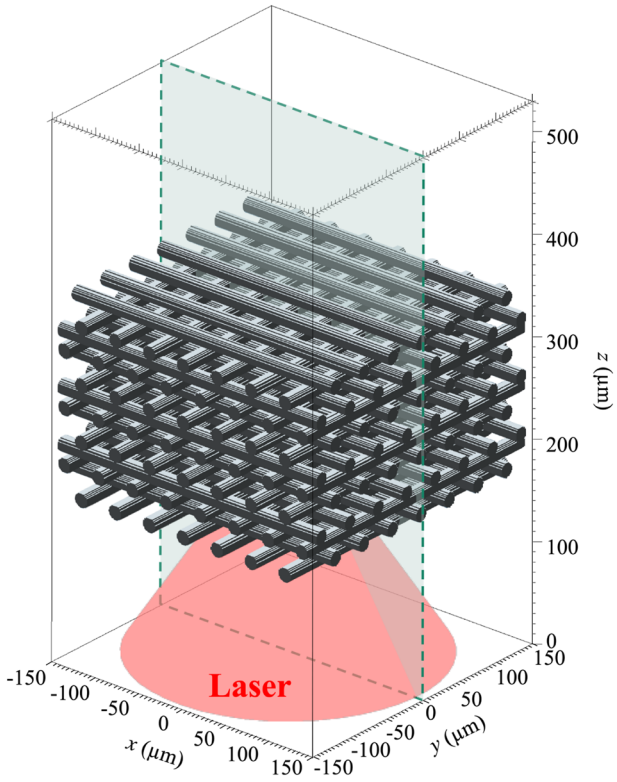

FIG. 3. Initial configuration of simulation. The domain was 300 μm wide along the x and y axes and 530 μm wide along the z axis. The plane along which the domain has been cut to show the results of the simulations presented is shown with teal shading and a dashed outline.

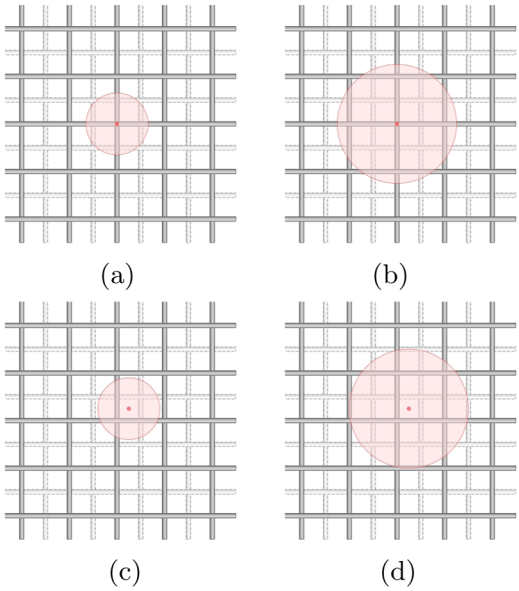

FIG. 4. Different focusing cases, with the light red shaded circle indicating the focal spot, and the red dot its center: (a) case 50C, 50 μm diameter spot with center at the crossing of filaments; (b) case 100C, same as 50C, but with a spot diameter of 100 μm; (c) case 50H, 50 μm diameter spot with center at the hole between the filaments of all layers; (d) case 100H, same as 50H, but with a spot diameter of 100 μm.

100 μm diameter spot with its center on the crossing of the filaments of the first layer; 50C, the same as 100C, but with a spot diameter of 50 μm; 100H, 100 μm diameter spot with its center on the through-hole between the filaments of all layers; 50H, the same as 100H, but with a spot diameter of 50 μm. Two more pointing possibilities can be considered. In the first, the center of the focal spot is placed on the crossing of the filaments on the second layer. This case is analogous to the "C" cases already described, although some modifications in the motion of the first layer will appear, since this is not directly irradiated as in those cases. The second possibility is the placement of the center of the focal spot on the middle point of a strut. We expect this case to be similar to the case with crossing, because, as discussed below, the peculiar feature of the "H" cases is the geometrical similarity between the material structure and the laser focusing, which causes channeling of the laser into the spaces. This condition can only be achieved when the center of the spot is close to the position of the "H" cases.

We performed one simulation for each case, to assess the importance of the pointing of the laser on the microstructure. The 50H and 100H simulations were initialized like the 50C and 100C simulations, but with the target shifted by a quarter of the period of the structure in both the x and y directions, keeping the laser direction along the central axis of the numerical domain. Figure 5 shows plots of the laser energy deposition, revealing the path of the laser rays as they traverse the microstructure after 0.1, 1, and 2.5 ns, the last of these corresponding to the time at which the laser pulse reached its maximum power. All the images in this figure and in Fig. 6 were obtained by slicing the numerical domain with a plane passing through the axis of the laser and normal to the x axis.

In cases 50H and 100H, laser scattering into the structure due to refraction by the plasma is seen. The large focusing angle of the $f/1$ lens makes part of the beam impinge on the target at an angle that facilitates scattering in a specific direction in the microstructure, forming a channel, as clearly seen for the 50H case. The heating resulting from this scattering is volumetric and affects all the layers of the material. The scattering is more broadly realized in case 100H because of the larger number of filaments and holes covered by the focal spot. At later times, as can be seen in the pictures for case 50H at 1 ns and for case 100H at 2.5 ns in Fig. 5, zones of highly inhomogeneous plasma density appear, leading to refraction of the laser rays into a small volume, which may result in self-focusing. In fact, as discussed below, the expansion and ablation of the thick filaments leaves zones of high density in the plasma until the end of the simulation at 10 ns. This may be the cause of the strong two-plasmon decay signature we observed in the experiments; see Sec. V C. In the cases of focusing on the crossing between filaments, namely 100C and 50C, the scattering is less evident and the heating depth in the target is similar. In these cases, the geometrical factors that favor the scattering in cases 50H and 100H are not sufficiently well met, and the laser is not scattered into channels. The time required for the plasma to fill the gaps between the filaments, thus preventing the laser from penetrating the structure, was of about 500 ps in all cases.

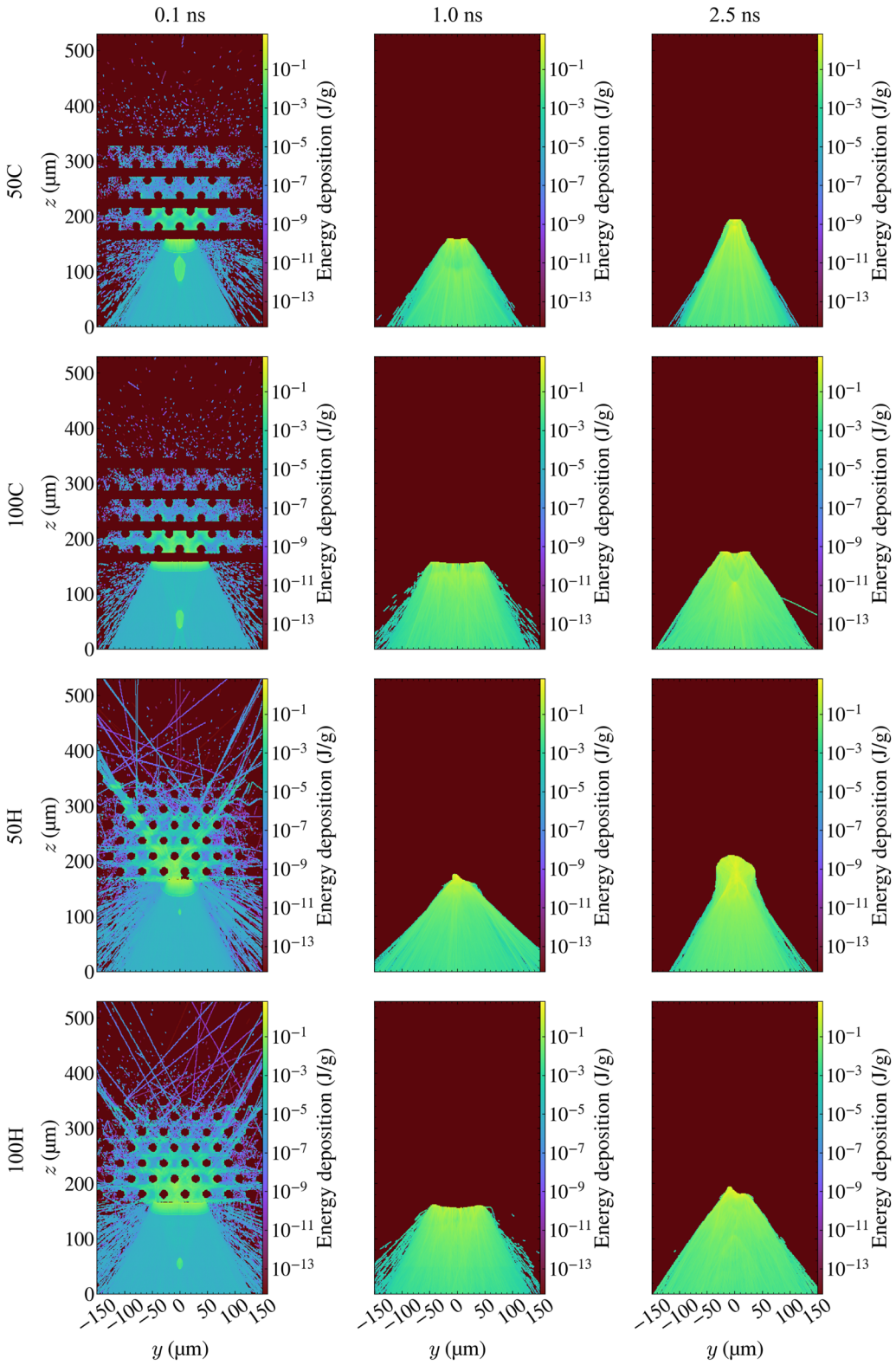

FIG. 5. Time evolution of laser propagation inside the microstructure. The columns show from left to right the times 0.1, 1, and 2.5 ns from the beginning of laser irradiation. For each time, the effect of the focusing of the laser is shown, from top to bottom, for cases 50C, 100C, 50H, and 100H.

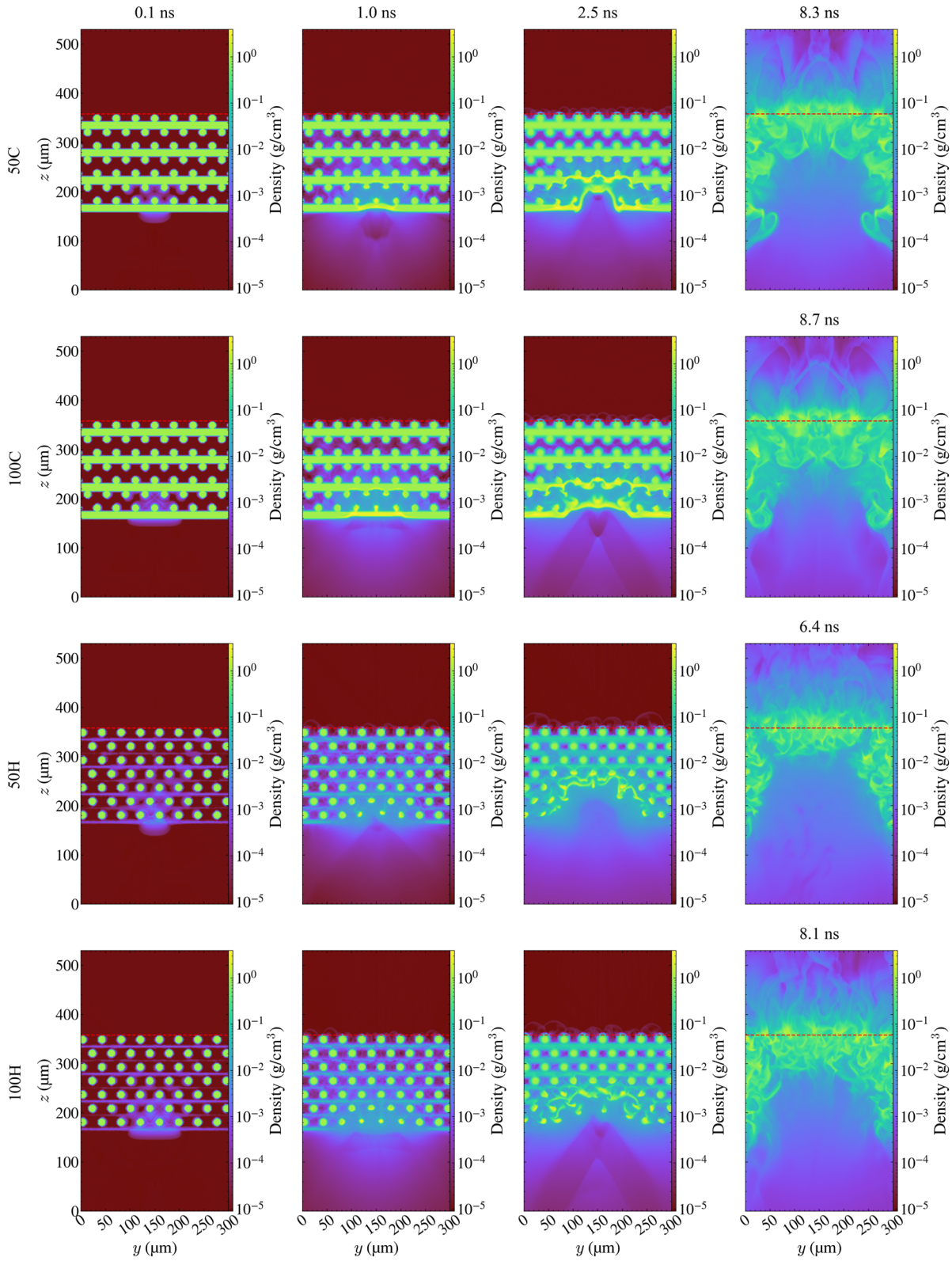

FIG. 6. Density plots at different times, depending on the focusing point on the structure. The red dashed line indicates the initial position of the back side of the target.

C. Erosion wave speed

Figure 6 shows the time evolution of the density of the target material and of the laser-generated plasma. We see that after 1 ns in cases 50C and 100C, the target structure remains almost intact, with shock waves propagating into the filaments of the first two layers. In these cases, we can also observe that the centers of the filaments of the first two layers are slightly displaced from their original position corresponding to the laser focal spot. This displacement is evident at 2.5 ns in case 50H at the peak of the laser power, where the two front layers have been completely ablated and displaced by the laser action. In case 100H, owing to the lower intensity, this process is slower, and the first two layers are starting to move and pack toward the rear side of the target. A different picture is seen in cases 100C and 50C, where at 2.5 ns we observe less displacement of the filaments, owing to the relatively shallower penetration of the laser into the structure, as observed in Fig. 5. The motion of the heated filaments appears to be more symmetric in the "C" cases than in the "H" cases. At the end of the laser pulse at 5 ns, the evolution of the material in cases 100C and 50C is similar, also considering the depth at which the target has been eroded by the laser action. From the images in Fig. 6, we can readily see that during the laser pulse, only partial homogeneity of the plasma is achieved. As discussed at the beginning of this section, this was expected, considering the very large thickness of the filaments and their large separation. From the simulation results, we estimated the breakout time of the erosion wave at the rear side of the target by the following procedure. Since we will be comparing the simulated speed of the erosion wave with the speed obtained from streak camera images, we calculated the total bremsstrahlung power emitted by the plasma $W_b \propto Z^3\rho\sqrt{T}$, where Z is the effective plasma ionization number, T is the plasma temperature, and ρ is the plasma density. We are omitting the proportionality constants, since we are interested in a qualitative analysis of this quantity. In general, the self-emission in the visible range from a point in the plasma is partially reabsorbed by the surrounding plasma itself. However, if we focus on the erosion wave breakout time, we can assume that the plasma density in the neighborhood of the breakout point is low, as confirmed by the simulations. In this approximation, the streak camera signal is proportional to the self-emission from the ejected plasma at the breakout point and is marginally affected by reabsorption. We extracted the profile of the total emitted bremsstrahlung power along 40 lines parallel to the y axis separated by 1 μm and at $z = 370$ μm. The value of the z coordinate corresponds to the position of the rear side of the target at $t = 0$ plus the diameter of a filament. The addition of the layer thickness to the z coordinate of the line is to further reduce the error in the measurement of the breakout time due to the surrounding plasma. The number of lines was chosen considering the 40 μm wide slit of the streak camera, as mentioned in Sec. III. Every 100 ps time, we computed the average of this quantity along all these lines individually and then averaged the result over all of them, and we identified the time at which this value reached the maximum. The time identified by this criterion was defined as the erosion wave breakout time. As can be seen in the last column of Fig. 6, the breakout time of the erosion wave is about the same for both 50 and 100 μm focal sizes when the axis of the laser beam is hitting the crossing of two filaments. There is a significant difference, on the other hand, between cases 50H and 100H. In the former case, we can identify two channels of low-density plasma, corresponding to the directions along which the laser was scattered (see Fig. 5 at 0.1 ns for case 50H). This rapid evaporation of material leads to a early time for breakout, which we can identify to be 6.4 ns in this last case. Case 100H is similar to 50H, but with a slower propagation of the erosion wave, which breaks out of the target at 8.1 ns.

TABLE I. Breakout times and average speeds of erosion wave obtained in different cases.

Focusing case	Breakout time (ns)	Speed (μm/ns)
50C	8.3	24.1
100C	8.7	23.0
50H	6.4	31.3
100H	8.1	24.7

As discussed in Sec. V, the breakout time was also measured experimentally. We have no information on the precise pointing of the laser for each shot from the experiments, and we cannot discriminate among the cases in Fig. 4. We can, however, reasonably assume that the most probable scenario is the one with the center of the focal spot located at intermediate position between the "C" and "H" cases. In fact, in the experiments, we did not care about the precise location of the center of the laser spot on the front layer of the target. In general, placing the center of the focal spot precisely on the crossing of the filaments in the experiments, as was done numerically for the "C" cases, would have been very challenging anyway. It is therefore reasonable to assume that the experimental result was close to an intermediate case. We can identify a maximum and a minimum expected average speed for the erosion wave, the former corresponding to the "H" cases and the latter to the "C" cases, in accordance with the above discussion. The obtained velocities are reported in Table I. As mentioned above, we also used the EoS obtained by the IONMIX code for polystyrene in the simulations. With this EoS, we obtained similar plasma profiles in all cases, even though the speed of the erosion wave was slightly different in the "C" cases. In particular, the speed for case 100C with the IONMIX EoS was 21.3 μm/ns and that for case 50C was 21.5 μm/ns, which were slower than those with SESAME 7592 by 1.7 and 2.6 μm/ns, respectively. On the other hand, as SESAME 7592 is more widely used and tested also with porous materials, we consider the results with this EoS more reliable.

V. EXPERIMENTAL RESULTS

A. Speed of erosion wave

The large thickness of the filaments and their large separation did not allow the plasma to reach homogeneity during the interaction, as the simulations reported in Sec. IV show. By using the streaked image from the side of the target, we were able to determine the average speed of the erosion wave into the sample, by following the same strategy used in Ref. 39. In Fig. 7, we show a typical example of a streaked image obtained during the experiments. To precisely locate the front and rear surfaces of the target, we performed a reference shot by damping the main beam before it entered the

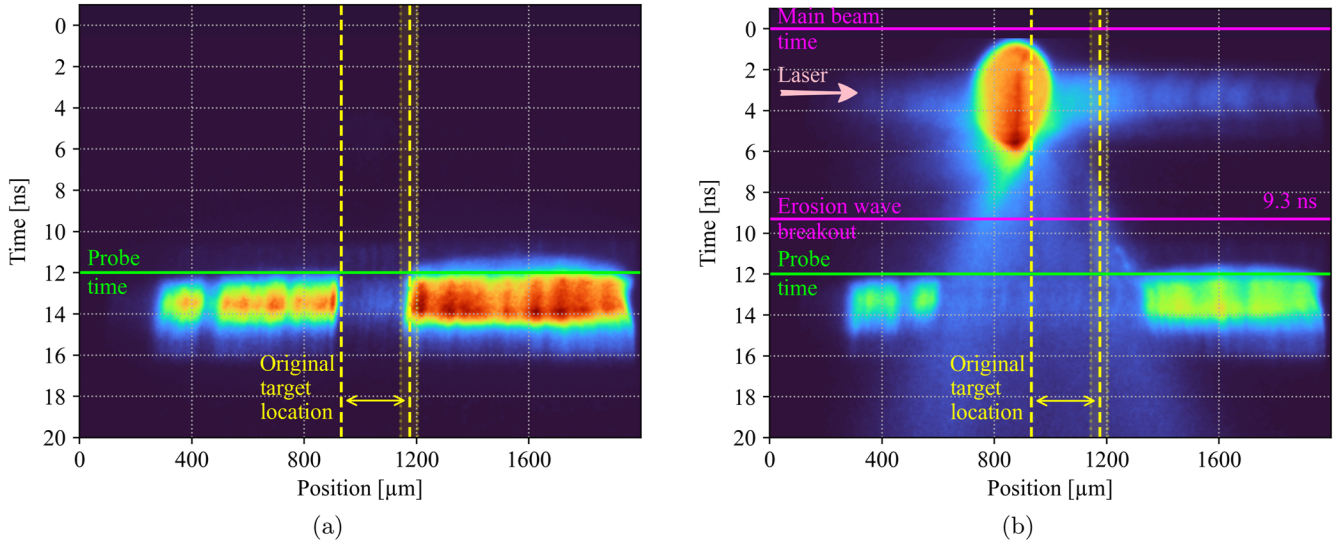

FIG. 7. Typical streaked image, obtained for shot 6416. (a) Reference shot made with only the probe beam, by damping the main one. (b) Streaked image of the shot, in which plasma self-emission is visible. The vertical yellow dashed lines identify the position of the target, the shaded yellow region indicates the error in estimating the position of the back of the target from (a), the horizontal green line indicates the time of the probe beam, and the purple horizontal lines in (b) indicate the time of arrival of the main beam on the target (upper line) and the time of erosion wave breakout (lower line). The main beam in (b) comes from the left of the image.

interaction chamber, thereby obtaining the result shown in Fig. 7(a). In this way, on the streak camera we obtained the shadow cast by the target on the probe beam and thus found the actual position of the target in the image. The error in the location of the rear side of the target has been estimated as the width of the rightmost shadow edge, indicated by the yellow shaded area between dotted lines in Fig. 7(a), giving 60 μm. Figure 7(b) shows the streaked image obtained during the irradiation by the main beam. As discussed in Sec. III, the probe beam reached the streak to be used as a fiducial. It is visible in both Figs. 7(a) and 7(b) with a 12 ns delay from the main beam, as indicated by the horizontal green line. From the streaked image, we can identify the instant at which the erosion wave reaches the rear side of the sample, by locating the first peak in the lineout of the image at the rear side location. We estimated the error on this measure by calculating the breakout times at the extrema of the edge of the shadow at the rear of the target, as obtained from the reference image, indicated by the yellow shaded area between dotted lines in Fig. 7. The breakout time for this shot was obtained as 9.3 ± 1.8 ns. The resulting average speed is of 27 ± 5 μm/ns. A similar procedure has been performed for the other shots. The blur at the self-emission front, which relates to the error in the speed measurement, is a direct consequence of the strong irregularities of the erosion wave front, also seen in the simulations in Sec. IV.

Figure 8 shows the results for several shots. The points in the plot, especially for the higher-intensity shots, show very good stability from shot to shot for the speed of the erosion wave. The measured velocity at about 1.5×10^{14} W/cm^2 was 25 μm/ns, while that for the shots around 7×10^{14} W/cm^2 was 29 μm/ns on average. Taking into account the errors in the experimental values, these measurements are within the ranges estimated from simulations, which are also reported in Fig. 8. In both cases, the speed is generally closer to the value obtained when the center of the focal spot was at the through hole in the microstructure, rather than at the crossing of the filaments in the first layer. This means that the dominant effect with a random pointing of the beam as in our experiments is the scattering

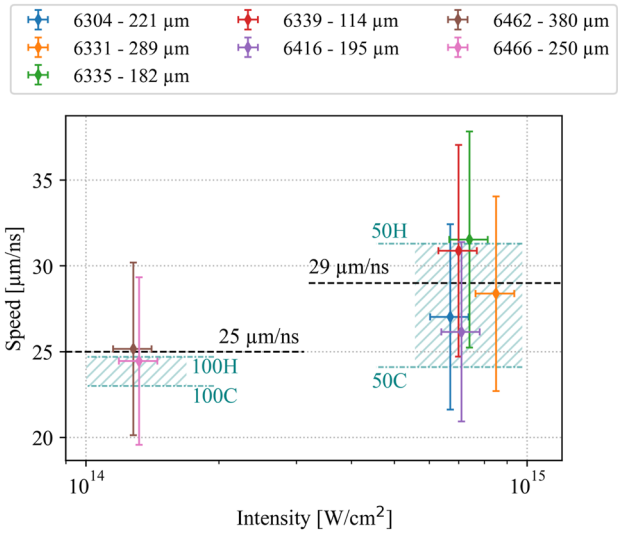

FIG. 8. Values of erosion wave speeds calculated from streaked images. The legend gives the shot number and the thickness of the target for each shot. The shaded areas correspond to the ranges of speeds obtained from the simulations for the two cases of higher and lower intensity, as indicated by the labels (see Table I).

of the laser light into the structure, leading in general to the effects observed in cases 100H and 50H described in Sec. IV. In these cases, the density gradients guide the laser into the voids of the structure more efficiently, thus leading to a faster wave.

B. Reflected and transmitted light

As explained in Sec. III, we recorded the time-resolved signals from two photodiodes, R and T, collecting the laser light reflected and transmitted by the target, respectively. For all the shots, we observed a negligible signal from photodiode T. This is consistent with the high average density of the sample and with the simulations. Figure 9 shows three typical signals from photodiode R recorded during the experiments, whose amplitude has been normalized to the maximum of the signal on photodiode L, which recorded the light from the main beam, for an appropriate comparison. The amplitude of the signals exhibited a very wide variability from shot to shot, probably due to large scattering and diffusion of the laser on the thick filaments and on the strongly inhomogeneous plasma, as can also be seen from the simulations in Sec. IV. Since we collected the reflected light through the $f/1$ focusing lens, covering a cone with an aperture of 50°, some of the light being diffused may have not been directed to the Photodiode R and therefore not detected. On the other hand, on average, the time duration of reflection was similar, as also seen from the same figure.

Figure 10 shows the integral of the reflected light signal from photodiode R normalized to the integral of the signal from photodiode L. In this plot, we indicate the shots performed at high intensity and those at low intensity. The red circles indicate the shots with a target of thickness lower than 150 μm, to determine how much the reduced thickness and a potential early erosion of the foam impacted on the reflection of the laser light. On average, the high-intensity shots tended to be less reflective than those at lower intensity. However, there seems to be no evident correlation between the thickness of the target, the laser intensity, and the reflectivity across the whole dataset. Since we changed the focal spot size to change the intensity, this is probably related to the scattering expected when the focal spot size is of the order of the separation between the filaments.

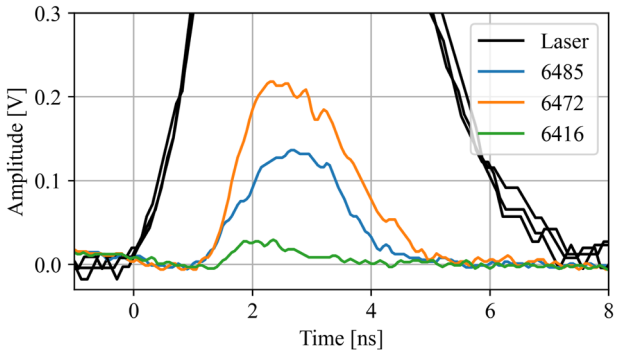

FIG. 9. Signals collected by photodiode R for some selected shots. These are indicated by the colored lines, while the black lines indicate the laser temporal profiles, as measured by photodiode L. The signals are normalized to the maximum of the laser temporal profile.

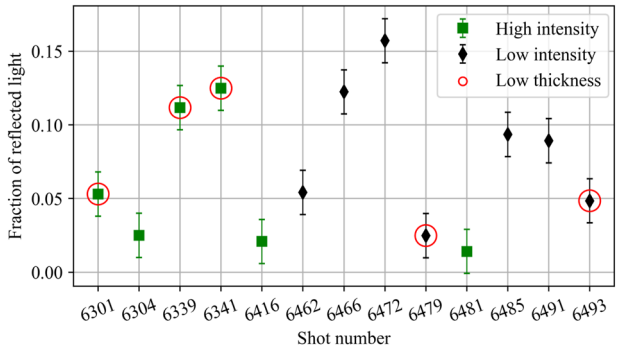

FIG. 10. Integrals of the signals from photodiode R, normalized to the integral of the signal from photodiode L for better comparison between the different shots. The points labeled "High intensity" are relative to the shots at about 7×10^{14} W/cm^2, while those labeled "Low intensity" had an intensity of 1.5×10^{14} W/cm^2. The red circles indicate the shots in which the target thickness was lower than 150 μm.

C. Laser–plasma instabilities

As indicated in Sec. III, a spectrometer was fielded in the experiment, watching the side of the target and collecting the self-emitted light from the plasma. Some of the shots had an unexpectedly high amplitude in correspondence to the signature of two-plasmon decay instability (TPD), i.e., the self-emission at $2\lambda_L/3$, λ_L being the laser wavelength. In our setup, this corresponds to $\lambda_{2/3} = 703$ nm.

Figure 11 shows some of the signals collected during the campaign. The signal amplitude exibited a large variability in the various shots. No clear correlation was found between the amplitude of the $2\lambda_L/3$ signal and the intensity in our dataset. High levels of TPD could be related to the creation of zones where the plasma density gradient caused self-focusing, because of the non-smooth density profile, as observed for the "H" cases in the simulations. Because of random beam pointing, the probability for this to happen was different from shot to shot, leading to the wide variation that we observed. Moreover, since the spectrometer was watching the plasma from the side, this may be due to some statistical slight tilting of the target, which may be shadowing the self-emission from the plasma in some cases. Therefore, we cannot use the amplitude as a quantitative estimate of the amount of self-emission and then of the amount of TPD,

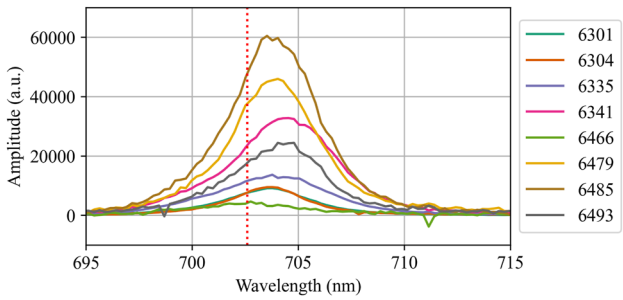

FIG. 11. Some of the signals collected by the spectrometer for the $2\lambda_L/3$ self-emission related to the TPD instability. In some shots, the signal was saturated and therefore these are not reported here. The vertical dashed red line corresponds to the exact value of $2\lambda_L/3$ for our experimental conditions.

but qualitatively we know that this instability has been active under our experimental conditions. For completeness, we note that Fig. 11 shows a clear shift of the emission at $2\lambda_L/3$ and a broadening. The shift of the maximum of the signals reported in the figure ranges from 0.8 to 1.8 nm toward longer wavelengths, meaning that only the effect from the red plasmon was detectable in our conditions. There is no clear explanation of this fact at the moment, and it will require further investigation. The detection of TPD suggests that other LPIs, such as stimulated Raman scattering (SRS) and stimulated Brillouin scattering (SBS) may also have been active under the present experimental conditions. We did not have dedicated diagnostics for the scattered light with the appropriate spectral range fielded in the experiment, and we cannot draw definitive conclusions on the effect of LPIs on the ablation pressure and flow evolution. Future experiments with tailored diagnostics, such as a full aperture backscatter station (FABS), would help in understanding the impact of all the instabilities on the interaction.

VI. CONCLUSIONS AND FUTURE DEVELOPMENTS

Understanding the physics at the basis of the plasma evolution in foams is very challenging, from both the theoretical and experimental points of view. In both cases, the randomness of the internal structure of a chemical foams has limited for decades our ability to probe the plasma within the material and also to properly simulate it. One of the main reasons of the great attention being paid to 3D-printed foams is the possibility of shaping their internal morphology, which is opening new ways of probing the plasma evolution and simulating the fundamental processes involved. In fact, simulating the behavior of a target with an ordered structure in a hydrodynamic code is much more feasible than reproducing the evolution of a stochastic net of filaments such as those present in chemical foams.[27]

This work represents one of the few numerical and experimental efforts[13,18,28,29] devoted to the study of the behavior of printed foams under irradiation. The structure of the samples used in this work was conceived to enable 3D simulations with a reasonable computational effort, widening the spatial scales involved. This allowed us to explore the evolution of the plasma in detail. As discussed in Sec. IV, under our conditions, no shock wave developed, because homogeneity of the foam was never reached. Rather, we observed the process of progressive destruction of the material, which we have called an erosion wave. The simulations also show that a regular structure with a large separation between filaments as in our samples leads to a fraction of laser energy being scattered inside the material at the beginning of the interaction. This leads to a peculiar behavior of the plasma, with the formation of zones where the erosion is more efficient, with a less smooth front of the erosion wave. The resolution of the mesh adopted in the simulations and the number of laser rays used in the ray tracing package proved to be adequate for the problem at hand, allowing appropriate resolution of the main physical processes at play.

By using visible streak camera images, we experimentally measured the average speed of the erosion wave, which proved to be in good agreement with the results of the simulations and well reproducible from sample to sample. This was possible thanks to the shot-to-shot stability of the ABC laser beam and to the high reproducibility of the structure of the material, which was nominally the same over the whole dataset. Owing to the large features of the samples, the error in the speed of the erosion wave was quite large, because of the blurring on the image at the time of breakout. A finer structure of the sample and a higher magnification for the streak camera image would reduce this uncertainty in future experiments. On the other hand, other observables, such as the reflected light, were not so reproducible from shot to shot. This was probably due to the impossibility of an exact pointing of the laser and to the similarity between the spot size (especially at high intensity) with the filament separation. The amplitude of the $3/2\omega_L$ self-emission related to TPD was also fluctuating, probably because of a non-optimal alignment of the target with the spectrometer. Other LPIs, such as SRS and SBS, may also have been active during the interaction, but no diagnostics were available to detect the related scattered light. The presence of hot electrons from TPD or SRS potentially pre-heating the sample may have been the reason for the faster erosion wave in the experiment compared with the simulations, where LPIs were not modeled. We therefore have no numerical or experimental data at our disposal to assess the influence of LPIs on the shock propagation or flow evolution, and dedicated experiments would be needed to confirm this supposition.

This work could be extended by using samples with a lower density, of 100 mg/cm^3 or below, with thinner filaments. This would increase the computational cost of the simulations, but it would be a reliable way of understanding the influence of the morphology on the features of the interaction. The effects on the plasma dynamics of a reduced spacing between filaments could also be explored. Experimentally, it should be possible to test the effect of a finer structure on the observables and their stability from shot to shot. We expect that the erosion wave that we have discussed will gradually turn into a well-defined shock wave as the filament thickness and the interfilament spacing are reduced. This will also help in reducing the error in the measured speed of the shock wave. A more well-defined front of the shock wave will give a sharper emission signal on the streak camera, allowing a more precise determination of the shock breakout time. LPIs are another point of interest in the physics of the interaction, and in future experiments a more detailed characterization will be needed, with dedicated diagnostics also for SRS and SBS, which were not available in the experiments presented in this work.

ACKNOWLEDGMENTS

This work has been carried out within the framework of the EUROfusion Consortium, funded by the European Union via the Euratom Research and Training Programme (Grant Agreement No. 101052200—EUROfusion). The views and opinions expressed are, however, those of the authors only and do not necessarily reflect those of the European Union or the European Commission. Neither the European Union nor the European Commission can be held responsible for them. The software used in this work was developed in part by the DOE NNSA- and DOE Office of Science-supported Flash Center for Computational Science at the University of Chicago and the University of Rochester. The computing resources and the related technical support used for this work have been provided by CRESCO-ENEAGRID High Performance Computing infrastructure and its staff.[33] The CRESCO-ENEAGRID High Performance

Computing infrastructure is funded by ENEA, the Italian National Agency for New Technologies, Energy and Sustainable Economic Development and by Italian and European research programmes; see http://www.cresco.enea.it/english for information. This research has been carried out in the framework of the "Universities' Excellence Initiative" programme by the Ministry of Education, Science and Sports of the Republic of Lithuania under an agreement with the Research Council of Lithuania (Project No. S-A-UEI-23-6). Additional support was received through EU LASERLAB-EUROPE JRA-extension (Grant Agreement No. 871124, Horizon 2020 Research and Innovation Programme).

AUTHOR DECLARATIONS

Conflict of Interest

The authors have no conflicts to disclose.

Author Contributions

M. Cipriani: Conceptualization (equal); Data curation (equal); Formal analysis (equal); Investigation (equal); Software (lead); Visualization (equal); Writing – original draft (lead); Writing – review & editing (equal). **F. Consoli**: Conceptualization (equal); Formal analysis (equal); Investigation (equal); Writing – review & editing (equal). **M. Scisció**: Conceptualization (equal); Formal analysis (equal); Investigation (equal); Writing – review & editing (equal). **A. Solovjovas**: Resources (equal); Visualization (equal); Writing – original draft (supporting). **I. A. Petsi**: Writing – review & editing (equal). **M. Malinauskas**: Conceptualization (equal); Resources (equal); Visualization (equal); Writing – original draft (supporting); Writing – review & editing (equal). **P. Andreoli**: Conceptualization (equal); Data curation (equal); Investigation (equal). **G. Cristofari**: Data curation (equal); Investigation (equal). **E. Di Ferdinando**: Data curation (equal); Investigation (equal). **G. Di Giorgio**: Data curation (equal); Investigation (equal).

DATA AVAILABILITY

The data that support the findings of this study are available from the corresponding author upon reasonable request.

APPENDIX A: TARGET FABRICATION

To produce the microstructures, we used two different fabrication systems: an Asiga Pico 2 UV 3D stereolithography printer operating at 385 nm central wavelength and a LDW MPL3DL utilizing the 515 nm wavelength. The full experimental setup is presented in Fig. 1. The holders for the structures were made by using the table-top 3D UV printer and Asiga Plasgray photo-resin, with a printing time of ~12 min. The samples were then dissolved in isopropyl alcohol to remove all nonpolymerized photo-resin. To fabricate the microstructures, we used SZ2080hybrid pre-polymer with the LDW system. In general, there are two options to prepare the solution for LDW fabrication, namely, to mix SZ2080 with 1% of Irgacure 369 photo-initiator or to use clean SZ2080 pre-polymer. The decision not to use the photo-initiator was made to reduce the amount of toxic ingredients in the process. The possibility of such green 3D printing, avoiding the mixing with photo-initiators, has recently been demonstrated.[40] In addition, the use of clean SZ2080 allowed us to avoid the presence of unwanted particles from the photo-initiator, which could result in bubble formation leading to micro-explosions during the formation of the structure. We also reduced the risk of bubble formation by cleaning the glass printing plate with isopropyl alcohol for a few minutes. To print the microstructure inside the already printed holder, we mounted the latter on a cover glass, and then drop-cast SZ2080 pre-polymer on it. After that, we annealed the sample for 100 min at 90 °C. During this process, the sample holder might start to curl owing to an increase of temperature, potentially causing detachment of the holder from the glass. In this case, printing is no longer possible because of severe degradation of the quality of the final product and the sample has to be discarded. For this reason, eight holders were annealed at once with SZ2080 pre-polymer to increase the success rate with a single printing. We also kept the wall thickness of the holder in the computer-aided design (CAD) model to be at least 400 μm, to avoid any deformation during drop-casting. For the LDW fabrication, we used an Yb:KGW laser (Pharos, Light Conversion, Ltd.) operating at 180 fs pulse duration, with 200 kHz pulse repetition rate and 1030 nm central wavelength. In addition, we used a beta barium borate (BBO) crystal to generate the second harmonic for the microfabrication process, for the wavelength to allow two-photon absorption in the SZ2080 resin. We focused the laser beam with a 0.8 numerical aperture objective. We modified the CAD model for the microstructure for every sample to compensate for any variation in the distance between the parts of the holder that had to support the microstructure with respect to the original one. In reality, this distance was found to vary from about 490 to 520 μm, and we had to allow the log-pile to extend about 50 μm more in the end, to ensure that the LDW printing started and ended on the holder supports, for better adhesion. The printing of the log-piles took from 60 to about 100 min, depending on the structure height and the writing speed. The most favorable laser power for this process was found to be between 0.2 and 0.3 mW (corresponding to 0.298 and 0.447 TW/cm^2 intensities at the focal spot within the sample volume), the power region at which SZ2080 polymerizes without micro-explosions. When the printing was completed, we cleaned the sample in a Petri glass filled with pentanone. We left the sample in the Petri glass for at least half an hour, to allow the sample holder with the microstructure to detach from the glass. This time had to be carefully controlled, to prevent the pentanone from dissolving too much of the sample holder, so that it would not stand straight.

APPENDIX B: STABILITY ANALYSIS OF SIMULATIONS

The stability of the results presented in Sec. IV was tested by changing the mesh resolution and the number of rays used in the ray tracing. The former is related to the accuracy of the simulation in reproducing the hydrodynamics for a single filament, while the latter could affect the reliability of describing the laser absorption and energy distribution because of laser scattering in a highly inhomogeneous material as is considered in this work.

1. Mesh resolution

The simulations presented in Sec. IV were performed with a mesh resolution of 1 μm in each spatial direction. We ran two more

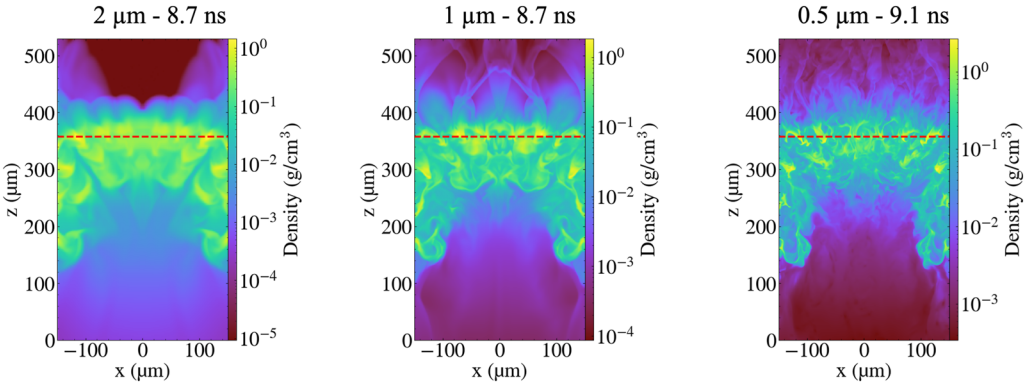

FIG. 12. Density at time of breakout for different mesh resolutions of 2, 1, and 0.5 μm from left to right.

simulations for case 100C, with resolutions of 2 and 0.5 μm, respectively, to determine the impact on the value of the erosion wave breakout time. The results are reported in Fig. 12. The plot with 2 μm resolution looks quite blurry compared with the one with 1 μm cell size, raising doubts about the accuracy in modeling the hydrodynamics for single filaments. However, applying the criterion for the estimation of the erosion wave speed described in Sec. IV, we find the same breakout time as with 1 μm resolution. This analysis suggests that this low resolution may be adequate for preliminary modeling of material evolution to obtain the overall behavior of the plasma, before adopting a higher resolution for definitive and more accurate results. With 0.5 μm resolution, we obtain a more detailed reproduction of the plasma shape compared with 1 μm cell size, as expected, but the general picture is not considerably different. We also get a slightly larger breakout time in this case, with the difference between the two values being about 4% of the values themselves. Even if, in principle, a higher mesh resolution would lead to more reliable results, the associated increase in the computational cost has to be considered: the simulation with 0.5 μm cell size took four times longer to run than the 1 μm one, with twice the number of CPUs, on the HPC supercomputer that we used. Considering that the experimental error has been estimated as 30%, as discussed in Sec. V A, and the reduced computational cost, we conclude that 1 μm resolution is the best compromise to obtain a reliable result in a reasonable computational time.

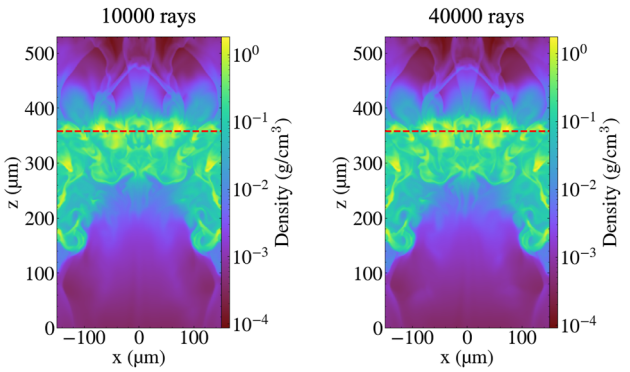

FIG. 13. Comparison between simulations with 10 000 (left) and 40 000 rays (right) for the ray tracing package.

2. Number of rays

As discussed in Sec. IV, we used 10 000 rays for the ray tracing. Given the complex scattering of the laser on the filaments in the early stages of the simulation, we used a large number of rays to increase the accuracy while keeping the computational time to a reasonable level. To check if this number of rays was enough to accurately resolve the dynamics of laser propagation and absorption into the target, we ran another simulation with 40 000 rays. As can be seen from the comparison shown in Fig. 13, changing the number of rays in the simulation did not affect the plasma evolution in an appreciable way. The time required for the simulation was not dramatically affected by the increase in the number of rays, increasing by a factor of about 1.5. We therefore conclude that 10 000 rays are a good value to reliably model the laser propagation with a reasonable computational time.

REFERENCES

[1] F. Pérez, J. R. Patterson, M. May, J. D. Colvin, M. M. Biener *et al.*, "Bright x-ray sources from laser irradiation of foams with high concentration of Ti," Phys. Plasmas **21**, 023102 (2014).

[2] A. Benuzzi, M. Koenig, J. Krishnan, B. Faral, W. Nazarov *et al.*, "Dynamics of laser produced shocks in foam–solid targets," Phys. Plasmas **5**, 2827–2829 (1998).

[3] D. Batani, A. Balducci, W. Nazarov, T. Löwer, T. Hall *et al.*, "Use of low-density foams as pressure amplifiers in equation-of-state experiments with laser-driven shock waves," Phys. Rev. E **63**, 046410 (2001).

[4] O. N. Rosmej, M. Gyrdymov, M. M. Günther, N. E. Andreev, P. Tavana *et al.*, "High-current laser-driven beams of relativistic electrons for high energy density research," Plasma Phys. Controlled Fusion **62**, 115024 (2020).

[5] M. Cipriani, S. Y. Gus'kov, F. Consoli, R. De Angelis, A. A. Rupasov *et al.*, "Time-dependent measurement of high-power laser light reflection by low-Z foam plasma," High Power Laser Sci. Eng. **9**, e40 (2021).

[6] S. Depierreux, C. Labaune, D. T. Michel, C. Stenz, P. Nicolaï *et al.*, "Laser smoothing and imprint reduction with a foam layer in the multikilojoule regime," Phys. Rev. Lett. **102**, 195005 (2009).

[7]R. De Angelis, F. Consoli, S. Y. Gus'kov, A. A. Rupasov, P. Andreoli *et al.*, "Laser-ablated loading of solid target through foams of overcritical density," Phys. Plasmas **22**, 072701 (2015).
[8]D. A. Mariscal, O. S. Jones, R. L. Berger, S. Patankar, K. L. Baker *et al.*, "Laser transport and backscatter in low-density SiO_2 and Ta_2O_5 foams," Phys. Plasmas **28**, 013106 (2021).
[9]L. Hudec, J. Limpouch, O. Renner, V. Tikhonchuk, R. Dudžák *et al.*, "Investigation of ion temperature in low-density undercritical foams," Plasma Phys. Controlled Fusion **67**, 025022 (2025).
[10]S. Iaquinta, P. Amendt, J. Milovich, E. Dewald, L. Divol *et al.*, "Characterization of foam-filled hohlraums for inertial fusion experiments," arXiv:2406.03475 [physics] (2024).
[11]A. S. Moore, N. B. Meezan, J. Milovich, S. Johnson, R. Heredia *et al.*, "Foam-lined hohlraum, inertial confinement fusion experiments on the national Ignition Facility," Phys. Rev. E **102**, 051201 (2020).
[12]R. E. Olson, M. J. Schmitt, B. M. Haines, G. E. Kemp, C. B. Yeamans *et al.*, "A polar direct drive liquid deuterium–tritium wetted foam target concept for inertial confinement fusion," Phys. Plasmas **28**, 122704 (2021).
[13]I. V. Igumenshchev, W. Theobald, C. Stoeckl, R. C. Shah, D. T. Bishel *et al.*, "Proof-of-principle experiment on the dynamic shell formation for inertial confinement fusion," Phys. Rev. Lett. **131**, 015102 (2023).
[14]K. Nagai, C. S. A. Musgrave, and W. Nazarov, "A review of low density porous materials used in laser plasma experiments," Phys. Plasmas **25**, 030501 (2018).
[15]H. Wang, W. Zhang, D. Ladika, H. Yu, D. Gailevičius *et al.*, "Two-photon polymerization lithography for optics and photonics: Fundamentals, materials, technologies, and applications," Adv. Funct. Mater. **33**, 2214211 (2023).
[16]E. Skliutas, G. Merkininkaitė, S. Maruo, W. Zhang, W. Chen *et al.*, "Multiphoton 3D lithography," Nat. Mat. Rev. Primers **5**, 15 (2025).
[17]T. Wiste, O. Maliuk, V. Tikhonchuk, T. Lastovicka, J. Homola *et al.*, "Additive manufactured foam targets for experiments on high-power laser–matter interaction," J. Appl. Phys. **133**, 043101 (2023).
[18]O. S. Jones, G. E. Kemp, S. H. Langer, B. J. Winjum, R. L. Berger *et al.*, "Experimental and calculational investigation of laser-heated additive manufactured foams," Phys. Plasmas **28**, 022709 (2021).
[19]T. Meier, R. Li, S. Mavrikos, B. Blankenship, Z. Vangelatos *et al.et al.*, "Obtaining auxetic and isotropic metamaterials in counterintuitive design spaces: An automated optimization approach and experimental characterization," npj Comput. Mater. **10**, 3 (2024).
[20]M. Hong, "Acousto-optic scanning multi-photon lithography with high printing rate," Opto-Electro. Adv. **7**, 240003 (2024).
[21]R. W. Paddock, M. W. von der Leyen, R. Aboushelbaya, P. A. Norreys, D. J. Chapman *et al.*, "Measuring the principal Hugoniot of inertial-confinement-fusion-relevant TMPTA plastic foams," Phys. Rev. E **107**, 025206 (2023).
[22]B. Albertazzi, P. Mabey, T. Michel, G. Rigon, J. R. Marquès *et al.*, "Triggering star formation: Experimental compression of a foam ball induced by Taylor–Sedov blast waves," Matter Radiat. Extremes **7**, 036902 (2022).
[23]J. Velechovsky, J. Limpouch, R. Liska, and V. Tikhonchuk, "Hydrodynamic modeling of laser interaction with micro-structured targets," Plasma Phys. Controlled Fusion **58**, 095004 (2016).
[24]M. Cipriani, S. Y. Gus'kov, R. De Angelis, F. Consoli, A. A. Rupasov *et al.*, "Laser-supported hydrothermal wave in low-dense porous substance," Laser Part. Beams **36**, 121–128 (2018).
[25]M. A. Belyaev, R. L. Berger, O. S. Jones, S. H. Langer, D. A. Mariscal *et al.*, "Laser propagation in a subcritical foam: Subgrid model," Phys. Plasmas **27**, 112710 (2020).
[26]L. Hudec, A. Gintrand, J. Limpouch, R. Liska, S. Shekhanov *et al.*, "Hybrid ablation–expansion model for laser interaction with low-density foams," Phys. Plasmas **30**, 042704 (2023).
[27]J. L. Milovich, O. S. Jones, R. L. Berger, G. E. Kemp, J. S. Oakdale *et al.*, "Simulation studies of the interaction of laser radiation with additively manufactured foams," Plasma Phys. Controlled Fusion **63**, 055009 (2021).
[28]J. Limpouch, V. Tikhonchuk, O. Renner, S. Agarwal, T. Burian *et al.*, "Laser interaction with undercritical foams of different spatial structures," Matter Radiat. Extremes **10**, 017402 (2025).
[29]C. Parisuaña, M. P. Valdivia, V. Bouffetier, K. Kurzer-Ogul, G. Pérez-Callejo *et al.*, "Shock propagation in aerogel and TPP foams for inertial fusion energy target design," Phys. Plasmas **32**, 082707 (2025).
[30]R. S. Craxton, K. S. Anderson, T. R. Boehly, V. N. Goncharov, D. R. Harding *et al.*, "Direct-drive inertial confinement fusion: A review," Phys. Plasmas **22**, 110501 (2015).
[31]E. M. Campbell, T. C. Sangster, V. N. Goncharov, J. D. Zuegel, S. F. B. Morse *et al.*, "Direct-drive laser fusion: Status, plans and future," Philos. Trans. R. Soc., A **379**, 20200011 (2021).
[32]O. A. Hurricane, P. K. Patel, R. Betti, D. H. Froula, S. P. Regan *et al.*, "Physics principles of inertial confinement fusion and U.S. program overview," Rev. Mod. Phys. **95**, 025005 (2023).
[33]F. Iannone, F. Ambrosino, G. Bracco, M. De Rosa, A. Funel *et al.*, "CRESCO ENEA HPC clusters: A working example of a multifabric GPFS spectrum scale layout," in *2019 International Conference on High Performance Computing Simulation (HPCS)* (IEEE, 2019), pp. 1051–1052.
[34]B. Fryxell, K. Olson, P. Ricker, F. X. Timmes, M. Zingale *et al.*, "FLASH: An adaptive mesh hydrodynamics code for modeling astrophysical thermonuclear flashes," Astrophys. J., Suppl. Ser. **131**, 273–334 (2000).
[35]A. Dubey, K. Antypas, M. K. Ganapathy, L. B. Reid, K. Riley *et al.*, "Extensible component-based architecture for FLASH, a massively parallel, multiphysics simulation code," Parallel Comput. **35**, 512–522 (2009).
[36]S. Lyon and J. Johnson, "SESAME 7592, in Los Alamos National Laboratory," Technical Report No. LA-UR-92-3407, 1995.
[37]J. J. Macfarlane, "IONMIX - A code for computing the equation of state and radiative properties of LTE and non-LTE plasmas," Comput. Phys. Commun. **56**, 259–278 (1989).
[38]See https://aphysics2.lanl.gov/apps/ for TOPS Opacities.
[39]M. Cipriani, S. Y. Gus'kov, R. De Angelis, F. Consoli, A. A. Rupasov *et al.*, "Laser-driven hydrothermal wave speed in low-Z foam of overcritical density," Phys. Plasmas **25**, 092704 (2018).
[40]D. Ladika, A. Butkus, V. Melissinaki, E. Skliutas, E. Kabouraki *et al.*, "X-photon 3D lithography by fs-oscillators: Wavelength-independent and photoinitiator-free," Light: Adv. Manuf. **5**, 567–579 (2024).